Comparison of Area-averaged and Local Boiling Curves in Pool and Jet Impingement Boiling

Preeti Mani, Ruander Cardenas, Vinod Narayanan*

204 Rogers Hall, School of Mechanical, Industrial, and Manufacturing Engineering, Oregon State University, Corvallis, OR 97331

**Corresponding author:* vinod.narayanan@oregonstate.edu

Abstract

Characterization of local boiling trends, in addition to the typically reported area-averaged trends, is essential for the robust design and implementation of phase change technologies to sensitive heat transfer applications such as electronics cooling. This paper compares local and area-averaged boiling curves during a phase change process using non-intrusive quantitative infrared thermal visualization to highlight the importance of considering the former in design of phase change cooling systems. As an illustration, both pool and jet impingement boiling modes of heat transfer from a heated silicon surface are considered. A thin-film serpentine heater that allows for a circumferentially uniform but radially non-uniform heat flux distribution on the surface is chosen as the heat source in order to assess the effect of spatial variations in imposed boundary condition on the local and area-averaged boiling curves.

Local convective heat fluxes are estimated from thermal maps using a control volume approach that accounts for axial conduction in the silicon substrate. Using the spatial information on surface temperatures and convective heat fluxes, local boiling curves are generated for different radial locations on the surface and compared with their corresponding area-averaged representations. As validation, it is shown that the net input electrical heat flux varies within 4 to 12 percent of the area-averaged results. Boiling curves averaged over regions of like imposed boundary condition are seen to provide a more realistic estimate of the local heat transfer conditions when compared with an area-averaged representation of the entire surface. Area-averaged thin-film sensor data are used to augment the heat transfer data by highlighting the differences in nucleation events on the surface in different regions.

Keywords:

Boiling; Jet impingement; Infrared thermography; Local boiling curves; Thin-film sensors; Probability distribution function

1. Introduction

Phase change cooling methods are being considered in thermal management of high-power electronic devices and components owing to the high heat transfer coefficients associated with phase change. Along with the need to dissipate high heat fluxes ($q'' \sim 10^6$-10^7 W/m^2), these electronic devices typically require maintaining surface temperatures lower than about 85°C. Over the years, several means of affecting phase change thermal management have been widely studied such as direct immersion phase change (Bhavnani et al., 2001), jet or spray impingement boiling (Mudawar and Wadsworth 1991; Robinson and Schnitzler 2007; Bernadin and Mudawar 1997; Horacek et al., 2005; Shedd 2007; Kim 2007) and microchannel flow boiling (Qu and Mudawar 2003; Hetsroni et al., 2006; Chen and Garimella 2011). Detailed reviews by Mudawar (2001) and Bar-Cohen et al., (2006) summarize the research developments and application potential of these thermal management schemes.

Implementation of phase change liquid cooling technologies to an electronic system needs accommodation of the sensitivity of these electronic devices to the stringent surface temperature constraints. For this reason, it is essential to fully characterize the performance of the cooling scheme. Boiling heat transfer performance is typically quantified in a plot of surface heat flux against the surface excess temperature that drives the heterogeneous phase change, which is commonly known as a boiling curve. Typically, a single boiling curve that is representative of the spatially averaged heat transfer performance of the phase change scheme is provided. While area-averaged trends provide valuable information on the heat transfer characteristics of the cooling scheme, it is also important to assess local variations in heat transfer rates. These local variations are particularly evident in forced convective flows such as that in a channel flow or in jet impingement, wherein the hydrodynamics and/or local variation in fluid temperature affects local heat transfer rates. In addition, for multi-chip electronics modules, there exist non-uniformities in the heat flux and surface temperatures that are not adequately captured by an area-averaged boiling curve. While the importance of determining spatially local or sectional representation of boiling performance is clear, such characterization involves evaluation of local values of surface temperature, which necessitates the use of multiple point sensors or the use of quantitative visualization methods. Hence, a large majority of literature on performance characterization of phase change cooling schemes is restricted to area-averaged results.

A common way to estimate an area-averaged boiling curve is to use a heater block with a heating source such as cartridge or thick-film heaters and axially located thermocouples. The test surface or channel is placed on the top of this heating block and the sides of the block are thoroughly insulated. A 1-D conduction model is used to determine the surface temperature and surface heat flux, which in turn provides an area-averaged boiling curve. Such a scheme has been used effectively in pool boiling (for

example, Jones et al., 2009), jet and spray impingement boiling (for example, Ma and Bergles 1986; Cardenas and Narayanan 2011; Chen et al., 2002) and in microchannel flow boiling (for example, Qu and Mudawar 2003).

There exist far fewer studies on spatially localized estimation of boiling curves and heat transfer coefficients in literature. Localized RTDs or thin-film sensors have been used successfully in the past to obtain spatio-temporal variations in temperature and heat transfer coefficients. In conjunction with high-speed imaging, the sensor data has been used in estimating the contribution of different mechanisms to boiling heat transport (Demiray and Kim 2004, Moghaddam and Kiger 2009) under single nucleating bubbles. In the latter study (Moghaddam and Kiger 2009), a plot of heat flux against surface temperature over a section of the heated substrate was used to illustrate the differences in heat transfer within and outside the bubble contact area.

Very recently, Chen and Garimella (2011) demonstrated the use of diode temperature sensors to obtain local boiling curves along the length of a microchannel heat sink during flow boiling in the context of identifying the thermal performance impact of flow instabilities in microchannels. Twenty five calibrated diode temperature sensors each embedded in a 2.54×2.54 mm^2 heating element were evenly distributed on a 12.7×12.7 mm^2 substrate housing 60 parallel microchannels. The net heat transferred to the fluid was estimated from the input heat flux by subtracting the heat flux in the absence of the fluid. This net flux and sensor temperatures were used to generate the local boiling and heat transfer coefficient curves along the microchannel. Regions downstream of the channel were found to change phase at lower wall temperatures than upstream of the channel. Severe fluctuations in the heat transfer coefficients in these regions were indicative of varying flow patterns like bubbly, slug, annular or churn flow. Transition from single-phase to pulsating phase change flow in the upstream channel regions was found to occur alongside the onset of flow instabilities leading to an enhanced heat transfer rate. The middle regions of the channel were found to maintain an almost constant heat transfer rate over the entire range of heat fluxes.

Thermal visualization methods like liquid crystal thermometry or infrared (IR) thermography have been used to determine the transient variations in temperature over entire spatial regions during phase change heat transfer (Kenning and Yan 1996, Muwanga and Hassan 2006, Krebs et al., 2010). Dukle and Hollingsworth (1996 a,b) used liquid crystal imaging to locate the areas of single-phase jet convection and nucleate boiling for a 5°C subcooled submerged jet impinging on a uniform heat flux surface. Nozzle-to-surface distances of 8.2 and 2.3 were chosen for which monotonic single-phase heat transfer distribution and a secondary peak in single-phase heat transfer occur respectively. Single point

temperature measurements were obtained at three locations using RTDs that sensed an area of 2.5×1.5 mm^2. The electrical current required to heat the metallic foil substrate and the voltage drop across each RTD were recorded to evaluate the net heat flux entering the test fluid. Boiling curves at the locations specified by the three RTD in conjunction with the corresponding liquid crystal thermal images were used to isolate regions that were cooled by forced convective jet flow and by phase change heat transport. Large temperature gradient associated with the interface of these two regions was reported. The authors noted that for the larger nozzle spacing, at any particular heat flux preceding complete nucleate boiling on the surface, the boiling front was stabilized by the large monotonic surface temperature gradients produced by the jet flow. In contrast, the non-monotonic surface temperature distribution set up at a closer spacing resulted in a collapse of the boiling front in the region of the secondary peak in surface temperature. The salient conclusion of their work was that the circumferentially-averaged boiling front location in the wall jet region can be predicted by single-phase heat transfer distribution.

Theofanous et al. (2002) used IR thermography to determine area-averaged boiling curves while characterizing pool boiling heat transfer of water on titanium coated sapphire substrate with a spatial resolution of 250 μm/pixel at 1kHz. Calibrated surface temperatures over a 1000 frames were averaged over the entire imaged heater area to evaluate the surface excess temperatures. These excess temperatures along with the input electrical heat flux were used to generate area-averaged boiling curves over the heater surface. In conjunction with X-ray radiography the nucleation site densities were also predicted. The superheats in regions of active nucleation sites were observed to be comparatively much lower than in the inactive regions. In a similar study, Gerardi et al. (2010) employed simultaneous IR and high-speed visualization to obtain time and space resolved 2D temperature distribution under nucleating bubbles during pool boiling of water under saturated conditions. A 30×10 mm^2 sapphire substrate was electrically heated using an ITO heater. Heat fluxes were estimated from the measured values of voltage and current during the experimental run. These input electrical heat flux estimates along with the IR temperature maps were used to obtain area-averaged boiling curves over an approximate area of ~5×5 mm^2.

More recently Ozer et al. (2011) employed quantitative liquid crystal thermography to obtain local temperature measurements on the upper surface of a microchannel during flow boiling. Simultaneously acquired high-speed images aided the determination of bubble size evolution and nucleation site density. A conduction model executed in ANSYS Fluent was used to correct for the local surface heat flux values based on the recorded wall temperatures. Construction of local boiling curves along the microchannel based on the recorded temperatures and estimated local values of heat flux were demonstrated.

The above past efforts to characterize spatially local heat transfer performance, be it in the form of boiling curves or heat transfer coefficients, support the fact that knowledge of local heat transfer characteristics is essential to the conceptual understanding and practical implementation of flow boiling heat transfer systems. In the current work, a comparison between local and area-averaged boiling curves is explicitly made to clearly highlight their differences. Two particular scenarios are considered to illustrate the importance of local boiling curves. The first corresponds to that of pool boiling on a silicon surface, wherein there is no imposed forced convective flow to cause spatial variations in addition to those that exist due to the randomly located nucleation sites. However, a non-uniform heat flux is imposed using a thin-film serpentine heater that provides a circumferentially uniform but radially non-uniform heat flux distribution on the surface. Such a scenario would be encountered in direct immersion cooling of multi-chip electronics modules, wherein the regions in between the modules are unheated. The second scenario is that of an imposed forced convective jet on the silicon surface. In this case, variations due to the imposed non-uniform heat flux as well as the convective flow are used to further highlight the differences between local and area-averaged boiling trends. Infrared thermography is used to obtain thermal maps and local heat fluxes are estimated using a simple two-dimensional conduction model. The validity of the local boiling curves is determined by comparing the area-averaged local results with the net input electrical heat flux measured during the experiment.

2. Test Section and Experimental Facility

2.1 Silicon Substrate Fabrication

Figure 1 shows an image of the thin-film heater and sensors. The heater pattern resulted in three concentric rings where joule heating was applied. The rest of the silicon (Si) surface was unheated and a circular jet was caused to impinge at the center of the concentric rings. The integrated heater and temperature sensors were fabricated on a 76.2 mm diameter double side polished p-type (111) silicon wafer of thickness, t = 380 μm. The wafer had a 2 μm thermally grown silicon dioxide layer on either side for electrical isolation and surface protection. The surface roughness of this oxide layer was estimated using atomic force microscopy to be 0.87 nm. The substrate was thoroughly cleaned with acetone, isopropyl alcohol and de-ionized water and blow-dried. Following this, one side of the substrate was spin coated with Shipley 1818 photo-resist and soft baked for 2 minutes. A Mylar mask was used for a photolithographic transfer of the pattern onto the resist coated side of the wafer. Microposit 351 was used to develop the pattern that served as a defining mask for the subsequent thermal evaporation of 1.2 μm of aluminum. Finally, the wafer was immersed in acetone overnight followed with ultrasonication to lift-off

metal from the unwanted regions. A layer of conductive silver paint was applied on the heater leads to minimize contact resistance between the pins and the heater. The area occupied by the heaters was painted flat black in order to increase the emissivity of the heater side of the wafer for the IR measurements. As mentioned later, a detailed in-situ calibration was performed to determine surface temperatures from the recorded thermal maps.

2.2 Substrate Mount

In order to mount the silicon substrate to a stainless steel test chamber, a custom polycarbonate holder (Fig. 2) was designed. The holder design was such that it permitted IR visualization from the backside (heater side) of the wafer. The substrate was clamped down into its groove in the holder with a 0.26 mm thin, circular polycarbonate clamp (inner diameter of 50.8 mm) that was chamfered inwards at a 25 degree angle to provide minimal obstruction to the jet flow. An o-ring located below the substrate provided the necessary seal to make the mount leak proof. Pogo pins were used to make electrical contacts to the heaters and sensors. The holder assembly was then mounted into the test chamber with the help of a flange. The lip of the polycarbonate holder was pressed against an o-ring on the chamber in order to form a seal. The test chamber was equipped with clear polycarbonate windows on three faces to permit flow visualization.

2.3 Test Facility

Figure 3 provides a simplified schematic of the experimental facility used for jet impingement boiling studies. The facility was built around the central test chamber housing the test section and consisted of (a) pool temperature control loop, (b) vapor condensation loop (c) jet flow loop and (d) data acquisition sub-system.

Pool temperature was maintained using a sub-loop that consisted of a pump and a heat exchanger. A recirculating heater/chiller provided the necessary heating/cooling to the heat exchanger. In addition to the recirculating chiller, two 550-watt cartridge heaters immersed in the pool were used to autonomously adjust the temperature of the pool through a PID controller. Pool temperature was monitored at two locations within the liquid in the chamber to verify a uniform temperature to within ±0.6˚C. Condensation coils located at the top back side of the test chamber were connected to a second recirculating chiller that provided chilled water at 5.5˚C to maintain proper condensation rates on the coil surface. The jet flow loop consisted of a variable-speed gear pump (Micropump) that supplied deionized, degassed water to the jet plenum in the test chamber (see Fig. 3). A Coriolis flowmeter (Micromotion Elite II) monitored the jet

mass flow rate. Two 250-watt cartridge heaters located just prior to the inlet of the chamber were used to control the jet temperature, which was measured inside the jet plenum. The flow exited a nozzle (inner diameter, d_{jet} = 1.16 mm) as a submerged circular jet that impinged on the circular heated Si substrate. A high current DC power supply (American Reliance Inc., Model SPS40-165-K0E7) was used to provide resistive heating to the aluminum heater. The pool temperatures and voltages from the thin-film sensors were monitored using a digital data acquisition system (National Instruments) using a LabVIEW program. The sensor voltages were recorded at a rate of 24 kHz.

2.4 Visualization Instrumentation

High-speed imaging and IR thermography were used in this study to visualize the phase change process. Bubble dynamics during boiling were qualitatively visualized with a Phantom V310 (Vision Research) camera at 9000 Hz and 30μs exposure time. The Phanton V310 camera is equipped with a 1280×800 pixel CMOS sensor with an active pixel size of 20μm and is capable of recording speeds in the range of 3.25 kHz to 500 kHz. A TVS 8500 IR camera (CMC Electronics) composed of a 236 pixel x 256 pixel InSb focal plane array sensor was used to record the thermal distribution at the silicon surface. The IR image resolution was estimated to be 230 micrometers per pixel based on the known width of the deposited aluminum heaters. Images of size ~54×59 mm^2 were recorded during steady state conditions at a frequency of 30 Hz.

3. Experimental Procedures

3.1 Data Collection Procedures

Experiments were performed at atmospheric pressure with deionized, degassed water as the working fluid. Prior to an experimental run, deionized water was boiled extensively inside a modified commercial water heater, which was used as a degassing chamber. The oxygen content of the degassed water was measured using a dissolved oxygen meter manufactured by Extech Instruments (Model 407510). The oxygen content measurement of the degassed water from the degassing chamber was lower than the accuracy error of the instrument (±0.4 ppm). The nozzle-to-surface spacing (standoff distance) was kept constant at 3.6 jet nozzle diameters. For pool boiling experiments, the flow rate to the nozzle was turned off. Prior to clamping the wafer onto the substrate mount (Fig. 2), the top surface of the wafer was thoroughly cleaned with acetone, isopropyl alcohol and deionized water.

Once the test chamber was filled, the deionized, degassed water was boiled again using the cartridge heaters to ensure further degassing of the test fluid. The heated pool of water was recirculated through the heat exchanger to maintain a 20˚C subcooling. The pool was initially mixed using the jet to ensure a uniform pool temperature. Three experiments were performed - one of pool boiling and two jet impingement conditions with jet exit Reynolds numbers, Re_{jet}, maintained at 2580 (jet exit velocity, v_{jet} = 0.81 m/s) and 5161 (v_{jet} = 1.6 m/s). Beginning from zero power, the current input from the DC power supply to the Si surface was incremented in steps of 0.4 A. At each power level, data collection was started once steady state was attained. High-speed videos, IR images and the pool and jet temperatures were recorded for each power level. The upper limit of heat flux was dictated by the voltage limits of the power supply.

3.2 Thermocouple and Surface Calibration for IR Thermography

Thermocouples for measuring the pool temperature were calibrated using a NIST-traceable RTD in a well-mixed oil bath. Previous studies by this group have shown that IR thermography requires a detailed calibration of the surface emissivity in order to determine a temperature from a recorded intensity (Patil and Narayanan 2005, Krebs et al. 2010). Following on the lines of these previous studies, an in-situ pixel-by-pixel calibration of the backside of the silicon wafer for IR thermography was performed.

The silicon wafer, with the heating area painted flat black, was mounted within the test chamber as in an actual experiment. The pool of deionized, degassed water was uniformly heated in the test chamber, and was monitored by the calibrated thermocouples. No electrical power was supplied to the wafer itself. Water was chosen as the working fluid for calibration to eliminate the possibility of oil residue causing contamination of the test chamber fluid and the silicon surface. Calibration was performed at six pool temperatures of 29˚C, 45˚C, 55˚C, 65˚C, 72˚C and 80˚C. At each steady state, pool temperatures and IR images from the rear side of the substrate were recorded simultaneously with the IR camera in the same position as for the three experimental cases. It should be noted that because the silicon surface was open to natural convection from the bottom side, the surface temperature was expected to be lower than that of the pool. However, since an in-situ calibration was performed, natural convection losses also occurred in the actual experimental run. Calculations for losses due to natural convection were nevertheless performed and verified their insignificance. Hence it was not deemed necessary to account for natural convection in either calibration or in the actual experiments.

Time-averaged calibration thermal maps were used to determine an appropriate calibration fit for each pixel of the thermal image, using the calibrated pool thermocouple temperatures as a reference.

Calibration fits thus obtained for each of the 60,416 pixels were used to obtain calibrated IR thermal maps providing quantitative surface temperature values.

4. Data Reduction and Uncertainty

4.1 Jet flow properties and IR data reduction

The exit velocity of the jet was computed from the mass flow rate measured by the Coriolis flow meter and the inner diameter of the jet nozzle. The computed exit velocity along with the liquid density and liquid viscosity, evaluated at the measured temperature, were then used to estimate the jet exit Reynolds numbers.

All the recorded IR images were converted to comma-separated-value (csv) format using PE Professional software (GORATEC) for further processing in MATLAB. At each power level and for each calibration temperature, thirty one consecutive thermal images were averaged pixel by pixel to create a time-averaged thermal image. Pixel calibrations were applied to all experimental IR data in order to generate calibrated thermal images. All images were cropped from their original size to an area of 150×150 pixels (~ 34.5×34.5 mm^2) corresponding to an area slightly larger than that of the heater rings.

Several approaches have been adopted to obtain heat flux in IR theromography experiments in literature. As described earlier in this article, Theofanous et al., (2002) and Gerardi et al. (2010) limited their use of IR imaging to obtain time and space resolved surface temperatures while their heat flux estimates were based on the measured input electrical flux. An alternative approach is to adopt a 2D conduction analysis to account for the axial conduction in the substrate and hence estimate the net convective heat flux from the recorded temperature maps. This approach has been previously implemented among others by Patil and Narayanan (2005) to compute local convective heat transfer coefficients from an impinging jet, and by Wagner and Stefan (2009) for obtaining heat fluxes under single nucleating bubbles. Heng et al., (2010) used an inverse heat transfer method to estimate upper surface temperature and heat flux in the context of single bubble nucleate boiling.

Since the primary intent of the present work is to compare local with area-averaged boiling curves, a 2D conduction analysis similar to that used by Wagner and Stefan (2009) is used to extract the local values of the heat flux from IR thermal maps. For such an analysis, the temperature drop across the thickness of the wafer due to conduction is neglected. Since the substrate is highly conductive (thermal conductivity, k = 149 W/m-K), accounting for axial conduction is more important than to account for change in

temperature through the 380 μm thickness of the wafer. For example, the highest averaged heat fluxes in this study (~7×10^5 W/m^2) would expect to see a temperature drop of about 1.8 °C across the 380 μm thick wafer, which can be accounted for as a bias error in the uncertainty estimate.

In order to reduce noise in the numerically computed conduction heat flux within the Si wafer, the calibrated time-averaged temperature images were passed through a top hat filter, which estimates the temperature value at each pixel (T_{filter}) based on a weighted average of its neighboring pixels,

$$T_{filter}(i,j) = \frac{1}{4}T(i,j) + \frac{1}{8}\left(T(i-1,j)+T(i,j-1)+T(i,j+1)+T(i+1,j)\right) + \frac{1}{16}\left(T(i-1,j-1)+T(i-1,j+1)+T(i+1,j-1)+T(i+1,j+1)\right) \quad (1)$$

A similar weighted-average filtering of thermal maps has been employed by Dutton et al. (2010) to reduce the uncertainties in recorded temperatures using liquid crystal thermometry. The filtered thermal image resulting from Eq. 1 is shown in Fig 4a.

A pixel-by-pixel control volume analysis was performed to determine the local convective heat flux. A binary representation of the serpentine heater pattern was generated (Fig. 4b) to determine the pixel locations at which the input electrical heat flux, $q''_{elec,Ah}$, was applied. This value of $q''_{elec,Ah}$ was estimated over the area occupied by the heater rings alone (Ah), based on the input voltage measured at the pins in contact with the thin-film heaters and the current measured at the power supply. For the present analysis each pixel (control volume) is defined to have a width, Δ = 230 μm, and a thickness, t = 380 μm, same as that of the Si wafer (Fig. 4c). The pixel width is defined for a square geometry such that $\Delta = \Delta x = \Delta y$. The control volume dimensions chosen here are based on the IR image resolution and are about 1.65 times smaller than the substrate width. To ensure that $\Delta > t$ would not significantly change the results, calculations for $\Delta = 1.2$ t, were done for pool boiling at the highest flux for a comparison. These calculations indicated that the average temperatures for the two cases were within 0.28 percent of each other, owing to the top-hat filtering process on the temperature maps. The corresponding differences in the computed convective heat fluxes were within 5.14 percent of each other.

At each control volume, an energy balance was performed (Fig. 4c) assuming steady state conditions with no energy storage. The convective heat flux, q''_{conv}, in locations with the serpentine heater (see Fig. 4b) was determined as,

$$q''_{conv}(i,j) = \frac{t\left(q''_{cond,x}(i,j) - q''_{cond,x}(i,j+1) + q''_{cond,y}(i,j) - q''_{cond,y}(i+1,j)\right) + q''_{elec,Ah}\,\Delta}{\Delta} \quad (2)$$

while in regions devoid of the heaters, q''_{conv} was estimated using Eq. 2 with $q''_{elec,Ah}$ set to zero. Accounting for the change in thermal conductivity of Si with temperature, the two-dimensional conduction heat flux, q''_{cond}, entering each pixel at the faces of the control volume in the x and y directions respectively, was computed using a central differencing scheme,

$$q''_{cond,x}(i,j) = -\left(\frac{k(i,j)+k(i,j-1)}{2}\right)\left(\frac{T_{filter}(i,j)-T_{filter}(i,j-1)}{\Delta x}\right) \quad (3a)$$

$$q''_{cond,y}(i,j) = -\left(\frac{k(i,j)+k(i-1,j)}{2}\right)\left(\frac{T_{filter}(i,j)-T_{filter}(i-1,j)}{\Delta y}\right) \quad (3b)$$

To eliminate noise in the convective heat flux estimated using Eq. 2, caused by the discrete nature of the temperature data, the estimated heat flux was subjected to three passes of a three sigma filter. This was followed by a 3-by-3 pixel local averaging at each pixel location to smooth out the data. The resulting convective heat flux spatial map within the region of interest is shown in Fig. 4d.

At this stage, boiling curves could be generated for each of the pixel locations within the region of interest shown in Fig. 4d. Symmetry afforded by the circular jet and the heater pattern was utilized to present a radially-local assessment of the heat transfer characteristics. The temperature (T_{filter}) shown in Fig. 4a and the flux (q''_{conv}) shown in Fig. 4d were circumferentially averaged for each radial location from the impingement point. Furthermore, in looking at the image of the heater in Fig. 4b, it becomes apparent that the upper semi-circular region of the serpentine heater is devoid of heater leads which cause local hot spots such as that seen in Fig. 4a. Hence, only the upper symmetric semi-circular region of the heaters (Fig. 4e) was chosen for computing the circumferentially averaged local surface temperatures, T(r), and convective heat fluxes, q''_{conv} (r). Figure 4e also indicates the specific heated sections (H1, H2 and H3) corresponding to the three heater rings and unheated sections (UH1, UH2, UH3) corresponding to the space between each heater ring for this upper semi-circular section. Sectionally-averaged boiling curves corresponding to these regions are provided in the results section. The convective heat flux corresponding to the upper semi-circular region is shown in Fig. 4f.

To obtain a global representation of the heat transfer characteristics from the local data, the circumferentially averaged temperature and convective heat flux were subjected to area-averaging beginning from the jet impingement point,

$$T_{avg}(r) = \frac{\{T(r)\cdot(2\pi r\Delta)\} + \{T_{avg}(r-1)\cdot(\pi\cdot(r-1)^2)\}}{\pi r^2} \quad (4)$$

$$q''_{conv,avg}(r) = \frac{\{q''_{conv}(r)\cdot(2\pi r\Delta)\} + \{q''_{conv,avg}(r-1)\cdot(\pi\cdot(r-1)^2)\}}{\pi r^2} \quad (5)$$

These values of T_{avg} (r) and $q''_{conv,avg}$ (r) describe the average surface temperatures and convective heat fluxes computed up to the radial distance, r, starting from the center point of the heater geometry. This manner of averaging the temperatures and heat fluxes allowed for the estimation of area-averaged quantities over the entire heater surface as well as sectional area-averaging over a specific range of radial locations such as those that encompass the heated ring or the unheated regions in between the rings and in the center.

The area-averaged heat flux results were compared with the net electrical input heat flux ($q''_{elec,net}$) for validation of the approach of estimating local heat fluxes. The net electrical heat flux was estimated as

$$q''_{elec,net} = q''_{elec,As} - conduction\,loss\ flux \quad (6)$$

Here $q''_{elec,As}$ represents the electrical heat flux computed over the substrate area corresponding to the serpentine heater. In Eq. 6, the conduction loss flux denotes the net conduction heat flux leaving the circumferential boundary of the outer ring of the heater in Fig. 4b. This value was computed based on the results of Eqs. 3a and 3b, circumferentially averaged for the three outer most radial locations on the heater. The computed values of $q''_{elec,net}$ for pool boiling were within 0.6-13 percent of $q''_{elec,As}$ for the entire range of fluxes tested.

The boiling curves presented here were subjected to a Locally Weighted Scatter-plot Smoothing (LOWESS) filter that performs a weighted least-squares regression of the data based on a specified span about the excess temperature. This filtering allows for a continuous representation of all raw data. Details of this filtering process can be found in Cardenas et al., (2011).

4.2 Thin-film sensor data

Voltages from two thin-film sensors, S_1 and S_2 (Fig. 1) were recorded at the steady state of each power level using LabVIEW at a rate of 24 kHz over a span of five seconds. As seen in Fig. 1, S_1 primarily measured the voltage drop on sections H1 and H2 of the heater while S_2 provided voltage drop measurements in the outer semi-circular section H3 of the heater. The data acquisition board limited the voltage readings to a ±20V range. Since resistance is a function of temperature, the drop in voltage over a

given area is also indicative of a drop in the local temperature at that instant of time caused by the departure of bubbles from the boiling surface. However it should be noted that in the present case, the recorded sensor voltage data represents a spatial average (over the sensor area) of multiple bubbling events at any instant in time. In order to interpret these drops in voltage, a probability distribution function (PDF) of such events was created for both sensors. Details of the sensor voltage time series and generation of the PDFs have been reported in Mani et al. (2011).

4.3 Uncertainty Estimates

Uncertainty in the temperature measurements can result from (a) the thermocouples used to measure the pool temperature during calibration (b) IR calibration and (c) curve fit error associated with the individual pixel calibration curves. The bias uncertainty associated with the thermocouples accounts for error due to calibration of the thermocouples against the NIST standard, NIST standard RTD error, and the thermocouple calibration curve fit error. This value was estimated to be ± 0.6°C. Precision error can arise whenever repetitive measurements are taken. The precision error associated with the thermocouples was calculated to be a maximum of 0.03°C. The net uncertainty in the thermocouple measurements was calculated by a root sum square of the thermocouple bias and precision errors, and found to be 0.6°C. The precision error associated with the IR camera noise was determined using 31 consecutive images recorded at each calibration temperature. The maximum precision error for a pixel temperature was found to be 0.04°C. The curve fit standard error resulting from the linear fit for each image pixel was found to have an average value of 0.34°C. Finally the total uncertainty in the IR temperature measurements were calculated by a root sum square of the net thermocouple uncertainty, the IR precision error and the IR standard curve fit error. The maximum overall uncertainty in heater surface temperature using IR thermography was 0.72°C. Uncertainty in the thin-film sensor measurements was attributed to the quantization error associated with the data acquisition board, which was 1mV. The net uncertainty estimates in the experimentally measured quantities are listed in Table 1.

The Kline and McClintock (1953) uncertainty estimate method was used to compute the uncertainties in T_{filter} (using Eq.1) based on bias and precision uncertainties on measured temperature values. A perturbation uncertainty analysis was performed on Eqs. 2 and 3 to propagate the uncertainties in T_{filter}, Δ, thermal conductivity, wafer thickness, heater area, T_{fluid}, voltage, and current, onto the local and the circumferentially averaged quantities. Averaged and maximum uncertainty percent estimates for these circumferentially averaged quantities for a range of heat fluxes are given in Table 2.

5. Results and Discussion

To demonstrate the differences between local and area-averaged boiling curves, experimental data were collected for one pool boiling condition $Re_{jet} = 0$ and two Re_{jet} of 2580 and 5161. The jet and pool temperatures were maintained at a 20°C subcooling through all three experimental runs.

Figure 5 compares the visualization results for pool boiling ($Re_{jet} = 0$) and jet impingement boiling ($Re_{jet} = 2580$), with increasing flux. Image sets (a) and (e) show the qualitative instantaneous high-speed images of boiling activity on the top side of the heated surface for the two test cases. Stationary bubbles, located at the periphery of the disk, remnant from degassing prior to the experiment, are seen in all of the high-speed images. The sets (b) and (f) show the quantitative time averaged filtered temperature maps on the back side of the heated silicon wafer. The IR images presented in this paper are oriented identical to the corresponding high-speed images presented, with the heater leads to the left. All the IR images have the same maximum and minimum scale for comparison. The set of images (i) compares the radial distribution of temperatures for pool and jet impingement boiling ($Re_{jet} = 2580$), starting from the jet impingement point, where r = 0. The temperatures along the y-axis in the plots are depicted as the circumferentially averaged temperatures T(r) in excess of the average subcooled fluid temperature (T_{fluid}). For jet impingement boiling, T_{fluid} was taken as the mean of the jet and pool temperatures measured during the experimental run.

For pool boiling (Figs. 5.1 (a) - 5.3 (a)), bubbles are seen to nucleate over the entire heated surface and the bubble density increases with increasing flux. It should be noted that although the glass nozzle is visible in the images, there was no jet flow under this condition. From the corresponding thermal images (Figs. 5.1 (b) - 5.3 (b)) and temperature difference profiles (open symbols, Figs 5.1 (i) - 5.3 (i)), it is clear that the surface is not at a uniform temperature. Since heat flux is provided in the concentric rings, the temperature is highest in the regions of the heater rings and heat is diffused axially within the silicon substrate towards the center, in between the concentric heater rings and at the edge of the heated region. Regions of high and low temperatures corresponding to locations of bubbles are also observed in thermal images in all heater rings and at all flux levels. This case of pool boiling is a clear example of how local variation in surface temperatures may be caused by the choice of thin-film heater geometry and due the distributed nucleation activity on the surface. Figures 5.1 (c) and 5.1 (d) present the PDFs of voltage drops of sensors S_1 and S_2 respectively, recorded for pool boiling at a flux of 2.3×10^5 W/m^2; while Figs. 5.3 (c) and 5.3 (d) represent the same for pool boiling at a flux 6.6×10^5 W/m^2. The area under each PDF is unity and hence PDFs are a normalized representation of a histogram of voltage drops. At any voltage interval (x-axis of the PDF), the magnitude of the PDF indicates the likelihood of the voltage drop being

in that voltage interval or bin. If the voltage drops indicate bubbling events, and the magnitude of the voltage drops indicate the number of bubbling events that were occurring at any instant in time, one would expect the PDF plots to be skewed towards more negative voltage bins with increase in flux (Mani et. al., 2011).

Higher number of boiling events are indicated by S_1 for both flux levels (Figs. 5.1 (c) and 5.3 (c)) since it covers a larger area than S_2 (Figs. 5.1 (d) and 5.3 (d)). At 2.3×10^5 W/m^2 voltage drops as much as -10V are observed in sensor S_1 with a significant number of these events occurring at voltage drops less than -3V. PDFs for S_2 at 2.3×10^5 W/m^2 are limited to voltage drops less than -4V. With increased flux the PDFs for both the sensors (Figs. 5.3 (c) and 5.3 (d)) shift towards more negative voltage bins indicating increased boiling activity on the surface. For S_1 at 2.3×10^5 W/m^2 the number of voltage drops in the range of -14V to -20 V is significant. The PDF of sensor S_2 also indicates the occurrence of boiling events in section H3 with a greater number of voltage drops with magnitudes less than -5V. From the presented visual and sensor results it can be concluded that for pool boiling, bubbles nucleate in, and depart from, all regions of the serpentine heater.

The series of images Figs. 5.1 (e) - 5.3 (e) represent high-speed visualization of the jet impingement boiling process for Re_{jet} = 2580 with progressively higher flux levels. For the fixed nozzle-to-surface distance of 3.6 jet diameters considered in this study, a monotonically decreasing single-phase heat transfer coefficient is expected during jet impingement with a global maximum at the impingement point. Bubble nucleation is initiated at the periphery of the heated surface (Figs. 5.1 (e) - 5.2 (e)) where the influence of the wall jet is diminished due to reduction in momentum of the wall jet, thereby resulting in higher surface temperatures radially outward from the impingement point (Figs. 5.1 (i) - 5.2 (i)). At a flux of 2.3×10^5 W/m^2 (Fig. 5.1 (e)), occasional bubbles are observed to nucleate and depart from the surface at a certain distance from the jet impingement point. The PDFs of sensor S_1 (Fig.5.1 (g)) for Re_{jet} = 2580 at this flux show much fewer boiling events with lower number of occurrences when compared with pool boiling (Fig.5.1 (c)). The voltage drops observed in S_1 are less than -8.5V. In comparison the probability of events in the vicinity of H3 is much higher as seen from the PDF of sensor S_2 for this case (Fig. 5.1 (h)). With further increase in flux, boiling activity increases and a more distinct ring of bubbles becomes visible (Fig. 5.2 (e)). At the highest flux (Fig. 5.3 (e)), a thicker ring of bubbles is observed, with an inward progression of the ring towards the impingement point. The PDFs of sensors S_1 (Fig. 5.3 (g)) and S_2 (Fig. 5.3 (h)) at the highest flux 6.6×10^5 W/m^2 for this test case corroborate the movement of boiling events inwards towards the jet impingement point as seen from the large negative voltage drops in the PDF of S_1 (~ -20V) compared to that of S_2 (~ -10V). Within the ring of bubbles, single-phase convective

heat transfer of the jet dominates while boiling heat transfer dominates in the region of the bubbles. For all fluxes of the Re_{jet} = 2580 case, the temperature difference profiles (Figs 5.1 (i) - 5.3 (i)) in the vicinity of the impingement region (UH1) suggest the existence of single-phase heat transfer. This spatial distribution of bubbles on the surface is responsible for the gradual knee in the boiling curve for jet impingement boiling as compared with pool boiling (Cardenas and Narayanan 2011).

When pool boiling is compared with jet impingement boiling at an identical flux level, pool boiling images depict that a large part of the heated surface is occupied by boiling activity while the presence of an impinging jet at the center of the heated area causes the boiling activity to shift to an off-center location. The thermal images for Re_{jet} = 2580 (Figs. 5.1 (f) - 5.3 (f)) and the corresponding temperature difference profiles (filled symbols 5.1 (i) - 5.3 (i)) corroborate the visual images. For the flux of 2.3×10^5 W/m^2a clear low temperature zone at the impingement point (r = 0) is observed in the thermal image (Fig. 5.1 (f)) as well as the temperature profile (Fig. 5.1 (i)) with temperature differences in the order of 10°C as opposed to pool boiling where temperatures differences are ~35°C . Circumferential variations in temperature for Re_{jet} = 2580 are negligible at this flux level of 2.3×10^5 W/m^2 with the highest surface temperature approximately equal to 43°C occurring at the inner edge of region H3. The temperature profiles (Fig. 5.1 (i)) of the pool boiling and Re_{jet} = 2580 cases corresponding to this flux level of 2.3×10^5 W/m^2 begin to merge beyond a radial location r of 0.009 m. This merging of temperature profiles suggests that the influence of the Re_{jet} = 2580 is limited to within r ~ 0.009 m (r/d_{jet}=7.84) from the impingement point. As the flux is increased to 2.9×10^5 W/m^2 (Fig. 5.2 (f)) thermal influence of the jet flow is seen to recede and some circumferential non-uniformities set in at the outer rings of the heaters due to the bubble thermal footprints. Regions of single-phase and phase change heat transfer are clearly distinguishable in the high-speed (Fig. 5.2 (e)) and the thermal image (Fig. 5.2 (f)) of the Re_{jet} = 2580 case. The temperature profiles (Fig. 5.2 (i)) also reflect this receding jet influence. As seen in Fig. 5.2 (i), the profiles of the pool boiling and Re_{jet} = 2580 cases begin merging at r ~ 0.008 m. With further increase in flux (Fig. 5.3 (f)) the boiling activity progresses inwards towards the impingement point. At the highest flux tested (6.6×10^5 W/m^2) three distinct bumps on each temperature profile (Fig. 5.3 (i)), corresponding to the three heater rings, are observed as a result of the non-uniform surface heating. The differences in temperature profiles of pool boiling and Re_{jet} = 2580 are notably diminished for r >0.004 m while single-phase persists for the Re_{jet} = 2580 test case at locations r <0.004 m (UH1). This trend is indicative of the decreasing spatial influence of the jet for Re_{jet} = 2580 and the increasing dominance of boiling over majority of the surface with increasing heat flux. Comparison of the PDFs obtained from sensors S_1 and S_2 for pool (Figs. 5.3 (c) and 5.3 (d)) and jet impingement (Figs. 5.3 (g) and 5.3 (h)) boiling at 6.6×10^5 W/m^2 shows little differences between the two cases indicating that boiling events are equally likely to

occur at locations H1, H2 and H3) for both test cases, which is in agreement with the merging temperature profiles (Fig. 5.3 (i)). As the regions of single-phase for Re_{jet} = 2580 are limited to within the unheated section UH1, the sensor S_1, which represents the heated sections H1 and H2, fails to capture the differences in boiling activity between pool and jet impingement boiling as observed in the high-speed and IR visualization images.

The spatial variations in temperature and regions of boiling activity caused due to the jet flow in addition to heater geometry emphasize the need to locally document the heat transfer behavior during phase change at different locations on a surface. While the use of sensors provides an estimate of the spatial variations, their representation is limited to the locations of the sensors. In the present case the sensors provide area-averaged estimates of boiling activity for only the heated sections of the surface. The following sections distinguish between heat transfer characteristics in the heated and unheated regions of the substrate, by use of the thermal maps and the determined heat flux.

5.1 Boiling Curve Validation-Comparison of $q''_{elec,net}$ and $q''_{conv, avg}$

Figure 6 shows the Lowess-filtered area-averaged boiling curves for the three test cases (filled symbols). The x-axis in this plot is represented as the area-averaged surface temperatures (T_{avg}) in excess of the average subcooled fluid temperature (T_{fluid}), which will henceforth be simply referred to as temperature difference. Overall the recorded jet and pool temperatures were within 0.2 - 0.8 percent of each other. Also plotted for comparison are the computed Lowess filtered values of the net input electrical flux $q''_{elec,net}$ (open symbols) calculated using Eq. 6 as a function of the area-averaged temperature difference. The unfiltered values of $q''_{elec,net}$ are marked in this plot as lines to illustrate the excellent agreement between the unfiltered and the Lowess filtered representations of the boiling curves.

Figure 6 shows good agreement between the net input electrical flux ($q''_{elec,net}$) with the experimentally obtained and analyzed convective heat flux values ($q''_{conv,avg}$), area-averaged over the entire heater surface for the three test cases. For the two jet impingement tests, the relative difference in the area-averaged heat flux results ($q''_{conv,avg}$) compared with the net input electrical flux ($q''_{elec,net}$) is estimated to be in the range of 4 - 5 percent, in the temperature difference range of 20 - 50°C. As a reference, the uncertainties in convective heat flux for pool boiling ranged from 5 - 11 percent for temperature differences of 20-50°C with the larger uncertainties occurring at the lower heat fluxes.

Figure 6 also summarizes the macroscopic behavior of the system as one would expect to see based on available area-averaged literature for pool and jet impingement boiling. Specifically, it is observed that

with increasing Re_{jet}, the magnitude of the heat transfer coefficient in the single-phase region increases, as denoted by the increasing slope of the boiling curves in the single-phase region. This increase in slope of the boiling curve in the single-phase region with an increase in jet flow rate is also indicative of an increase in the incipience boiling heat flux. With progressive increase of input heat flux both the jet impingement test cases tend to approach pool boiling behavior. It is to be noted that since the experiments were limited by the capacity of the power supply, critical heat flux was not attained in these experiments.

Area-averaged trends such as those mentioned above are useful in interpreting the general behavioral characteristics of phase change systems. However, it will be shown in later sections that these trends are not indicative of the local differences in heat transfer such as that caused by a forced convective jet flow or a non-uniform imposed heat flux.

5.2 Local boiling curves versus area-averaged boiling curves

To illustrate the inadequacies of an area-averaged heat transfer representation, Fig. 7 compares the local boiling curves in the presence of a forced convective jet flow (Re_{jet} = 5161), to the corresponding area-averaged boiling curve. The local boiling curves in Fig.7 are shown for six different radial locations situated at the center of each heater (H1, H2 and H3 in Fig. 4e) and non-heater sections (UH1, UH2, and UH3 in fig. 4e) on the surface, along a line of increasing radii. The local temperature difference values are obtained by subtracting the fluid temperature directly from the circumferentially averaged temperatures T(r). Similarly, the local flux values are obtained from the circumferential averaging of the jet convective flux, $q''_{conv}(r)$ at the specified radial location from the jet impingement point. The corresponding area-averaged values were obtained from Eqs. 4 and 5, and are denoted here by filled black circles.

As is evident from the plot, the heat transfer trends at each of the radial location depicted here are individually distinct. At radial locations $r = 1.76d_{jet}$ (between impingement point and inner heater ring, UH1) and $r = 4.51d_{jet}$ (center of the inner heater ring, H1), that are closer to the jet impingement point a significantly steep slope in the single-phase region of the boiling curve indicative of a high heat transfer coefficient is observed. This can be attributed to the forced convection of the jet that significantly enhances the single-phase performance at locations which are close to the stagnation point. However, the $q''_{conv,avg}$ severely under predicts the heat transfer coefficient in this region. In addition, notice that these two radial locations retain single-phase through the entire experimental run which is misrepresented by the area-averaged curve based on the phase change activity occurring in other regions of the test surface. While single-phase jet flow dominates heat transfer rate at these locations, the maximum $q''_{conv}(r)$ at the unheated location (UH1) of $r = 1.76\ d_{jet}$ is less than one half the maximum value at $r = 4.51d_{jet}$ which is at the center of the first heater ring (H1). This difference in maximum $q''_{conv}(r)$ clearly indicates the

consequence of a non-uniform imposed heat flux boundary condition such as that provided by the serpentine heater. As seen in Fig. 7, such a discrepancy between maximum q''_{conv} is noted between all heated an unheated sections.

Moving outward from the stagnation point to the location $r = 7.84d_{jet}$ (centered on the middle heater ring H2), trends in the boiling curve more akin to the area-averaged curve is observed. The local values of heat flux at this radial location fall within 0.2-20 percent of the averaged values for this experimental run, with the higher differences being exhibited at the larger temperature differences. The single-phase heat transfer coefficient at this location is reduced when compared with the inner regions and is consistent with the loss in momentum and thickening of the thermal boundary layer of the radially spreading wall jet. At higher temperature differences, phase change heat transfer occurs at this location as indicated by a change in slope of the boiling curve.

Further outward from the stagnation point at $r = 11.4d_{jet}$ (H3) the slope of the single-phase region and hence the heat transfer coefficient experience a larger drop. This is indicative of the diminishing influence of the jet at this large radial distance away from the stagnation point. The area-averaged values over predict the single-phase heat transfer coefficients at these locations, and depict a 4-5°C lower temperature difference for the onset of nucleate boiling. The corresponding spatial variations in surface temperature for a fixed convective heat flux is detrimental to the performance of electronic devices, which would exceed its temperature limits if the cooling system were designed using an area-averaged performance curve.

5.3 Comparison of Sectionally-averaged and Local Boiling Curves

The previous section clearly indicated that significant differences in the boiling curves exist between an area-averaged representation and a radially-local representation. These differences are caused in Fig. 7 due to both the flow field set up by the jet as well as the imposed heat flux boundary condition. The intent of this section is to determine whether averaging over sections with like boundary conditions (for example, uniform heat flux boundary condition in H1, H2 and H3 shown in Fig. 4e) provides an adequate representation of heat transfer performance within these sections or whether it is necessary to have higher spatial fidelity of boiling trends.

Figure 8 compares the performance of sectional area-averaged boiling curves with the local boiling curves within a specified region. This comparison is depicted for the H2 section during pool boiling (Fig. 8a), and for section H2 (Fig. 8b) and section H1 (Fig. 8c) during jet impingement at $Re_{jet} = 5161$.

Sectionally-averaged temperatures and convective heat fluxes were determined for the regions of interest using Eqs. 7 and 8

$$T_{savg}(b-a)=\frac{\left(T_{avg}(r)_{r=b}\cdot\pi b^2-T_{avg}(r)_{r=a}\cdot\pi a^2\right)}{\left(\pi\left(b^2-a^2\right)\right)} \tag{7}$$

$$q''_{savg}(b-a)=\frac{\left(q''_{conv,avg}(r)_{r=b}\cdot\pi b^2-q''_{conv,avg}(r)_{r=a}\cdot\pi a^2\right)}{\left(\pi\left(b^2-a^2\right)\right)} \tag{8}$$

where a and b represent the radial limits of the section. The radial span of each section was estimated from the binary representation of the heater depicted in Fig. 4e.

For pool boiling (Fig. 8a), few differences are observed in the single-phase region between the local and sectionally-averaged boiling curves while in the phase change region the curves begin to deviate with increasing heat flux. In the boiling region of the curves, the outer location (r/d_{jet} = 8.62) is seen to have a larger slope in the boiling curve than the inner location (r/d_{jet} = 7.05), indicative of a larger two-phase heat transfer coefficient. Substrate conduction estimates from H2 region at a fixed electrical power input of 440 W (corresponding to the highest flux data in Fig. 8a) indicated that the conduction flux out of the inner control volumes towards UH2 region was, on average, 12 percent larger than conduction out towards the UH3 region. Hence, in order to achieve the same convective heat flux as the outer or middle locations, the surface temperature at the inner radial location had to be larger than at other locations within H2. Alternately, for a fixed surface temperature, the inner locations on H2 showed lower convective heat fluxes. Irrespective of these differences between the local and sectionally-averaged curves, it is seen that the sectionally-averaged data provides a reasonable estimate of the local trends. In the single-phase region, the heat transfer coefficient variation between the local data and sectionally-averaged data shown in Fig. 8a was on average 8 percent with a maximum of 22 percent deviation from the sectional average for the inner location. In the phase change region of the boiling curve, at a fixed representative heat flux of 600,000 W/m^2, the local temperature differences were on average within 5.3 percent, with a maximum of 5.6 percent deviation from the sectionally-averaged temperature difference for the inner location.

Figure 8b presents the sectionally-averaged and local boiling curves for Re_{jet} = 5161 for the same H2 section as that shown for pool boiling in Fig. 8a. Similar to the pool boiling case, the inner location at r/d_{jet} = 7.05 is seen to have a lower slope in the single-phase region of the local boiling curve than does the sectional averaged curve or the outer region of r/d_{jet} = 8.62. This result might be seemingly

contradictory for jet impingement since in single-phase jet impingement, the heat transfer coefficient is larger for locations closer to the impingement point at these nozzle-to-surface spacings. The lower heat transfer coefficient at the inner location in this case is caused due to the stronger influence of substrate conduction heat loss, as explained for pool boiling, than that of the convective jet flow.

Figure 8c presents the comparison between sectionally-averaged and local boiling curves for Re_{jet} = 5161 on the heated section H1 which is the inner heater ring. It is to be noted that within this section, the heat transfer trends are distinctly in single-phase regime. As with the trends for the H2 section seen in Fig. 8b, the heat transfer coefficient in the inner location (r/d_{jet} = 3.72) is distinctly (by 17.7 percent) lower than the sectionally-averaged heat transfer coefficient. The reason for the seeming contradiction is much the same as that for the H2 section described above. Substrate conduction estimates from H1 region at a fixed electrical power input of 445 W (corresponding to the highest flux data in Fig. 8c) indicated that the conduction flux out of the inner control volumes towards UH1 region was, on average, 50 percent larger than conduction flux out towards the UH2 region.

For the present forced convective condition, sectional averaging provides reasonable estimates of boiling trends within the region of like boundary conditions. However, it should be noted that the percent difference between local and sectionally-averaged data would increase in the case of forced convective flows over large sectional areas.

5.4 Area-averaged versus Sectionally–averaged Trends

Based on the reasonably good agreement between sectionally-averaged curves and the local curves within regions of identical imposed boundary conditions (Fig. 8), a comparison is now made between sectional and area-averaged trends for pool boiling and jet impingement boiling (Re_{jet} = 5161). As mentioned previously, in pool boiling there is no forced convective flow to induce spatial temperature variations. However, spatial variations in the surface temperature may be observed due to an imposed non-uniform heat flux. Within each heater ring where electrical heating is supplied (H1, H2 and H3 in Fig. 4e), a uniformity in the heat flux boundary condition holds while in the unheated substrate regions UH1, UH2, and UH3, there is no imposed heat flux.

Figures 9a and 9b depict the pool boiling curves computed for locations on and off the serpentine heater rings respectively. For pool boiling with a non-uniform imposed heat flux, it is shown that trends in boiling curve averaged over regions of like imposed boundary condition provide a more realistic estimate of the local heat transfer conditions when compared with an area-averaged representation of the entire

surface. The maximum estimated heat flux in H1 and H2 regions (Fig. 9a) are 25 percent, and 21 percent larger than the estimated area-averaged heat flux respectively. However, the maximum heat flux in the H3 region (Fig. 9a) is seen to fall behind the average by 3 percent. This slight drop in H3 compared with the area-average is attributed to the radially outward conduction losses to the substrate experienced by the periphery of this region.

In contrast, sectional averages of the unheated sections (Fig. 9b) are consistently lower than the area-averaged values. The maximum estimated heat flux in UH1, UH2 and UH3 regions are 42 percent, 24 percent and 37 percent lower than the estimated area-averaged heat flux. It should be noted that while differences exist in heat flux magnitudes between sectionally-averaged and area-averaged boiling curves, the trends observed in the temperature difference along the x-axis are not significantly different.

Figures 9c and 9d compare sectional and area-averaged trends in the presence of an impinging jet (Re_{jet} = 5161) for the heated and non-heated sections of the substrate respectively. Similar to the case of pool boiling, the maximum estimated heat flux in H1 and H2 regions (Fig 9c) are 27 percent, 15 percent larger than the estimated area-averaged heat flux while H3 is lower by 2.8 percent. The sectional averages of the maximum estimated heat flux in the unheated regions UH1, UH2 and UH3 (Fig. 9d) are consistently lower than the estimated area-averaged heat flux by 33 percent, 27 percent and 30 percent respectively. In addition to the misrepresented heat fluxes as seen in pool boiling, Figs. 9c and 9d for the jet impingement case clearly depict that the area-averaged trends fail to capture the large spatial variations in surface temperature induced by the convective flow of the jet. For example, at a fixed representative heat flux of 600,000 W/m^2, the sectionally-averaged temperature differences on the heated sections H1, H2, and H3 (Fig. 9c) differed from the area-averaged value by 30 percent, 6.8 percent and 1.7 percent respectively. Another important upshot of such a comparison is that for phase change in the presence of a convective flow, the distinct regions of the single-phase and nucleate boiling as seen in Fig. 5 are lost in the area-averaged representation. These distinct regions of single and phase change flow, which occur during jet impingement partially developed nucleate boiling, are clearly identified with the aid of sectionally-averaged results.

With recent advances in non-intrusive and spatially-resolved thermal imaging, it has become possible to obtain data at several thousand points at once. It is shown here that by a judicious selection of regions that have like imposed boundary condition and well as small variations in convective flow boundary condition, it is possible to provide sectionally-averaged data that are representative of local variations in heat transfer data. Particular to the cases of pool boiling and jet impingement boiling presented in this

paper, it has been shown that nine sectionally-averaged curves can adequately represent local variations provided by ~7936 local points.

6. Conclusions

A quantitative comparison between area-averaged and radially-local boiling curves was presented in the context of pool boiling and jet impingement boiling on a polished silicon surface. The surface was heated by a concentric serpentine heater, which provided three sections with a circumferentially uniform heat flux and three sections with no imposed heating. By imposing a non-uniform heat flux boundary condition, and by introducing spatial variations in heat transfer coefficient with the aid of an impinging jet, it was shown that an area-averaged boiling curve fails to represent the spatial variations in boiling heat transfer. The spatial non-uniformity of nucleation events for pool boiling versus jet impingement boiling was qualitatively depicted with high-speed and infrared thermal images of the boiling process. Radial temperature profiles and PDFs of voltage drops obtained from thin-film sensors quantitatively corroborated the non-uniformity of nucleation events in different sections of the heated surface. Due to the vast amount of data and the ensuing difficulty in interpreting local boiling curves over the entire surface, sectionally-averaged representations of boiling curves were presented wherein sections of like imposed heat flux were analyzed. It was shown that if the sections are chosen such that they contain similar boundary conditions and are relatively small, sectional averaging can adequately represent local trends for both pool boiling and jet impingement boiling. It was demonstrated in this manuscript that such a sectionally-averaged heat transfer representation can substantially simplify the interpretation of data while retaining important information of local heat transfer variations over the heated surface.

7. Acknowledgment

The authors are grateful to the National Science Foundation for financially supporting this work under award number 0748249.

References

Bar-Cohen, A., Arik, M., Ohadi, M., 2006. Direct Liquid Cooling of High Flux Micro and Nano Electronic Components. Proceedings of the IEEE. 94 (8), 1549-1570.

Bernadin, J. D., Mudawar, I., 1997. Film boiling heat transfer of droplet streams and sprays. Int. J. Heat Mass Transfer 40 (11), 2579-2593.

Bhavnani, S. H., Fournelle, G., Jaeger, R. C., 2001. Immersion-Cooled Heat Sinks for Electronics: Insight from High-Speed Photography. IEEE Trans. Compon. Packag. Technol. 24 (2), 166-176.

Cardenas, R., Narayanan, V., 2011. Submerged jet impingement boiling of water under sub-atmospheric conditions. J. Heat Transfer 134, 020909-1-020909-8.

Cardenas, R., Mani, P., Narayanan, V., 2011. Sub-atmospheric mini-jet impingement boiling of water under saturated and subcooled conditions, Proceedings of ASME/JSME 2011 8th Thermal Engineering Joint Conference, AJTEC2011-44388, Honolulu, Hawaii, USA.

Chen, R. H., Chow, L. C., Navedo J. E., 2002. Effects of spray characteristics on critical heat flux in subcooled water spray cooling. Int. J. Heat Mass Transfer 45, 4033-4043.

Chen, T., Garimella, S. V., 2011. Local heat transfer distribution and effect of instabilities during flow boiling in a silicon microchannel heat sink. Int. J. Heat Mass Transfer 54, 3179-3190.

Demiray, F., Kim, J., 2004. Microscale heat transfer measurements during pool boiling of FC-72: effect of subcooling. Int. J. Heat Mass Transfer 47, 3257–3268.

Dukle, N. M., Hollingsworth, D. K., 1996a. Liquid crystal images of the transition from jet impingement convection to nucleate boiling part I: monotonic distribution of the convection coefficient. Exp. Thermal Fluid Sci. 12, 274-287.

Dukle, N. M., Hollingsworth, D. K., 1996b. Liquid crystal images of the transition from jet impingement convection to nucleate boiling part II: nonmonotonic distribution of the convection coefficient. Exp. Thermal Fluid Sci. 12, 288-297.

Dutton, T. W., Pate, L. R., Hollingsworth, D. K., 2010. Imaging of surface-tension-driven convection using liquid crystal thermography. J.Heat Transfer 132, 121601-1-121601-6.

Heng, Y., Mhamdi, A.,Wagner, E., Stephan, P., Marquardt, W., 2010. Estimation of local nucleate boiling heat flux using a three-dimensional transient heat conduction model. Inverse Probl. Sci. En. 18, 279-294.

Hetsroni, G., Mosyak, A., Pogrebnyak, E., Segal, Z., 2006. Periodic boiling in parallel micro-channels at low vapor quality. Int. J. Multiphase Flow 32, 1141-1159.

Horacek, B., Kiger, K. T., Kim, J., 2005. Single nozzle spray cooling heat transfer mechanisms. Int. J. Heat Mass Transfer 48, 1425-1438.

Jones, J. B., McHale, J. P., Garimella, S. V., 2009. The influence of surface roughness on nucleate pool boiling heat transfer. J. Heat Transfer 131, 121009-1-121009-14.

Kenning, D. B. R., Yan, Y. Y., 1996. Pool boiling heat transfer on a thin plate: features revealed by liquid crystal thermography. Int. J. Heat Mass Transfer 39 (15), 3117-3137.

Kim, J., 2007. Spray cooling heat transfer: The state of the art. Int. J. Heat and Fluid Flow 28 (4), 753-767.

Kline, S. J., McClintock, F. A., 1953. Describing uncertainties in single-sample experiments. Mech. Eng. 75, 3–8.

Krebs, D., Narayanan, V., Liburdy, J., Pence, D., 2010, Spatially resolved wall temperature measurements during flow boiling in microchannels. Exp. Thermal Fluid Sci. 34, 434–445.

Gerardi, C., Buongiorno, J., Hu, L. W., McKrell, T., 2010. Study of bubble growth in water pool boiling through synchronized, infrared thermometry and high speed video. Int. J. Heat Mass Transfer 53, 4185-4192.

Ma, C. F., Bergles, A. E., 1986. Jet impingement nucleate boiling. Int. J. Heat Mass Transfer 29 (8), 1095-1101.

Mani, P., Cardenas, R., Narayanan, V., 2011. Submerged jet impingement boiling on a polished silicon surface. Proceedings of ASME 2011 Pacific Rim Technical Conference and Exposition on Packaging and Integration of Electronic and Photonic Systems, Interpack2011-52042, Portland, OR, USA.

Moghaddam, S., Kiger, K., 2009. Physical mechanisms of heat transfer during single bubble nucleate boiling of FC-72 under saturated conditions – I. Experimental investigation. Int. J. Heat Mass Transfer 52, 1284-1294.

Mudawar, I., 2001. Assessment of High-Heat-Flux Thermal Management Schemes. IEEE Trans. Compon. Packag. Technol. 24 (2), 122-141.

Mudawar, I., Wadsworth, D. C., 1991. Critical heat flux from a simulated electronic chip to a confined rectangular impinging jet of dielectric liquid. Int. J. Heat Mass Transf. 34, 1465–1480.

Muwanga, R., Hassan, I., 2006. Local heat transfer measurements in microchannels using liquid crystal thermography: methodology development and validation. J. Heat Transfer 128, 617-626.

Ozer, A. B., Oncel, A. F., Hollingsworth, D. K., Witte L. C., 2011. A method of concurrent thermographic–photographic visualization of flow boiling in a minichannel. Exp. Thermal Fluid Sci. 35, 1522-1529.

Patil, V.A., Narayanan, V., 2005. Spatially resolved heat transfer rates in an impinging circular microscale jet. Microscale Thermophys. Eng. 9, 183–197.

Qu, W., Mudawar, I., 2003. Flow boiling heat transfer in two-phase micro-channel heat sinks—I. Experimental investigation and assessment of correlation methods. Int. J. Heat Mass Transfer 46, 2755-2771.

Robinson, A. J., Schnitzler, E., 2007. An experimental investigation of free and submerged miniature liquid jet array heat transfer. Exp. Thermal Fluid Sci. 32 (1), 1–13.

Shedd, T. A., 2007. Next Generation Spray Cooling: High Heat Flux Management in Compact Spaces. Heat Trans. Eng. 28 (2), 87-92.

Theofanous, T. G., Tu, J. P., Dinh, A. T., Dinh, T. N., 2002. The boiling crisis phenomenon Part I: nucleation and nucleate boiling heat transfer. Exp. Thermal Fluid Sci. 26 (6), 775–792.

Wagner, E., Stephan, P., 2009. High-resolution measurements at nucleate boiling of pure FC-84 and FC-3284 and its binary mixtures. J. Heat Transfer-Trans. ASME 131(12), 121008-1 -121008-12.

Tables and Figures

Table 1 Uncertainty estimates of measured quantities

Quantity	Average Uncertainty
Pool Temperature	±0.6°C
Jet Temperature	±0.6°C
Jet Flow Rate	±0.99 g/min
Jet Exit Velocity	±0.03 m/s
Reynolds number	2.2 percent
Current	±0.3 percent
Voltage	±0.75 percent
Sensor Voltage	±1 mV

Table 2 Uncertainty estimates for circumferentially averaged quantities (Re_{jet} = 0)

$q''_{elec,Ah}$ W/m^2	Uncertainty Estimate	T(r) [%]	T(r)-T_{fluid} [%]	q''_{conv} (r) [%]
3.4×10^3	**Average**	0.23	33.54	4.16
	Maximum	0.23	55.64	5.58
19.3×10^3	**Average**	0.21	7.48	2.95
	Maximum	0.22	12.58	4.47
79×10^3	**Average**	0.18	2.42	2.76
	Maximum	0.20	4.26	6.04
23×10^4	**Average**	0.15	1.51	2.95
	Maximum	0.17	1.96	15.79
29×10^4	**Average**	0.15	1.44	2.88
	Maximum	0.16	1.84	17.97
43×10^4	**Average**	0.15	1.38	2.53
	Maximum	0.16	1.74	12.48
66×10^4	**Average**	0.15	1.35	2.14
	Maximum	0.17	1.88	6.60

Figure 1

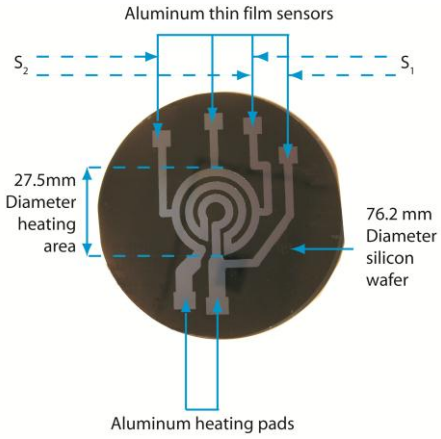
Aluminum thin film sensors
S2
S1
27.5mm Diameter heating area
76.2 mm Diameter silicon wafer
Aluminum heating pads

Figure 2

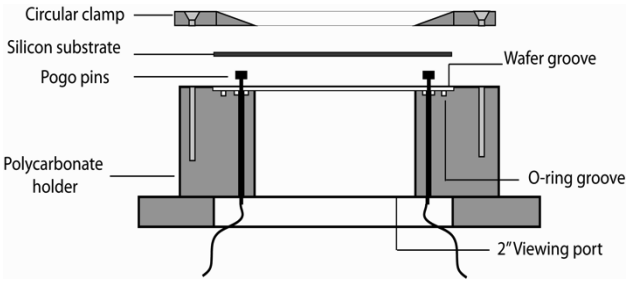
Circular clamp
Silicon substrate
Pogo pins
Wafer groove
Polycarbonate holder
O-ring groove
2"Viewing port

Figure 3

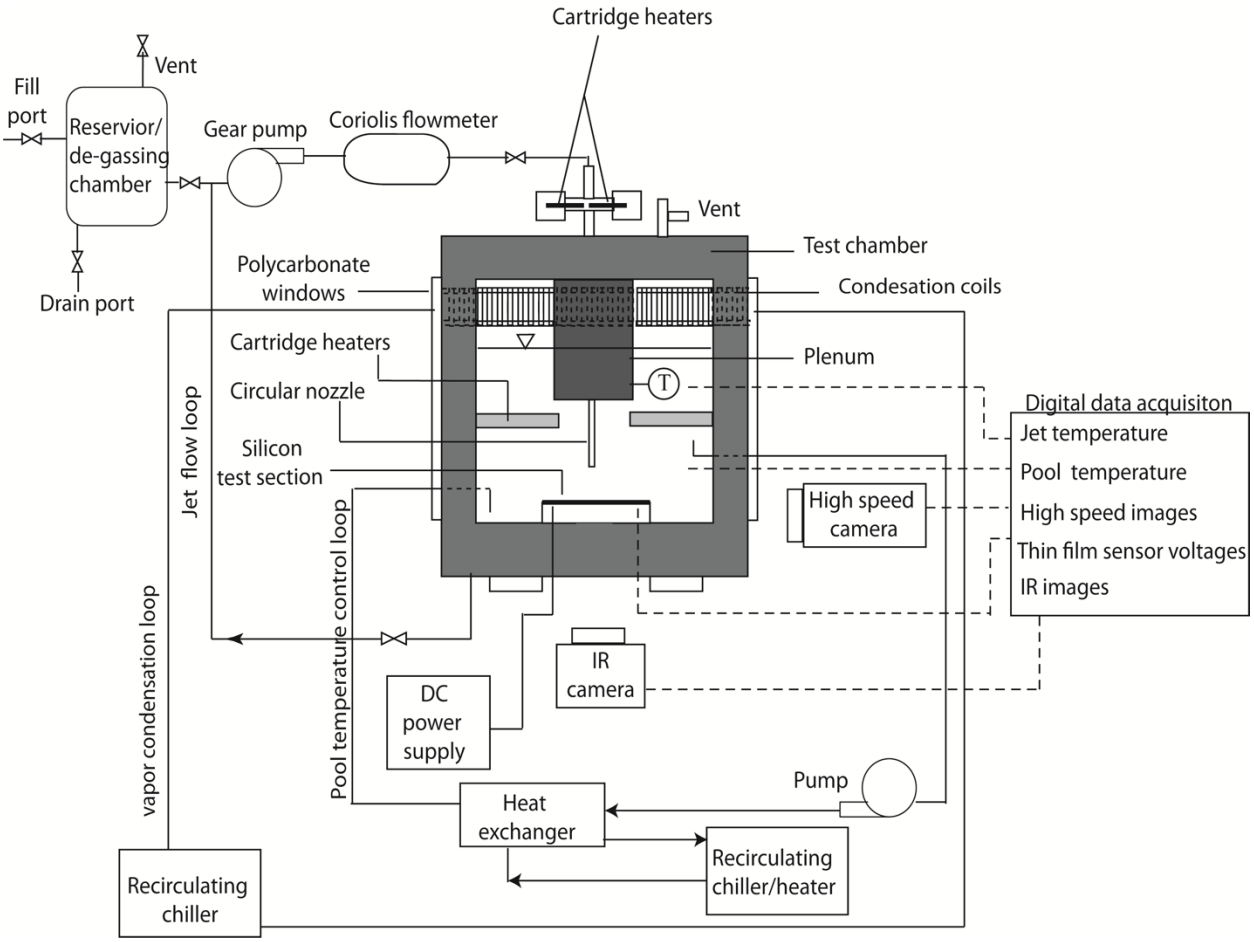
Cartridge heaters
Vent
Fill port
Reservior/ de-gassing chamber
Gear pump
Coriolis flowmeter
Vent
Test chamber
Polycarbonate windows
Condesation coils
Drain port
Cartridge heaters
Plenum
Circular nozzle
T
Digital data acquisiton
Jet temperature
Pool temperature
High speed images
Thin film sensor voltages
IR images
Silicon test section
High speed camera
Jet flow loop
Pool temperature control loop
vapor condensation loop
IR camera
DC power supply
Pump
Heat exchanger
Recirculating chiller/heater
Recirculating chiller

Figure 4

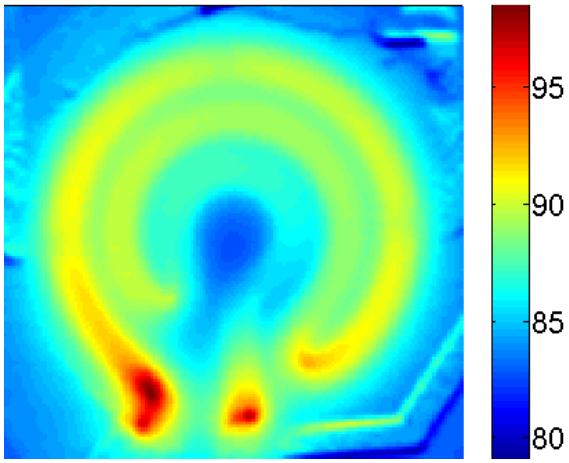

(a)

(b)

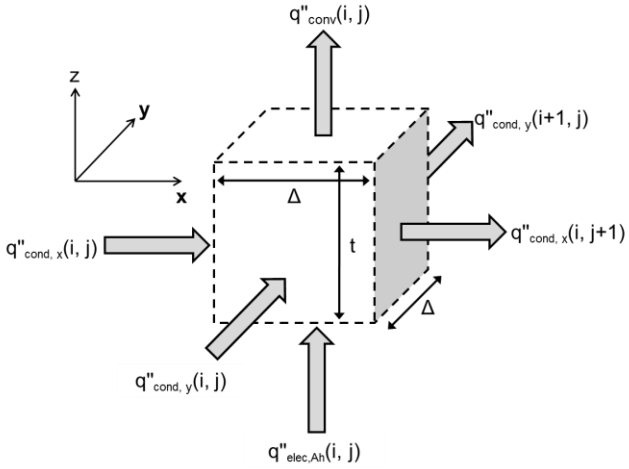

(c)

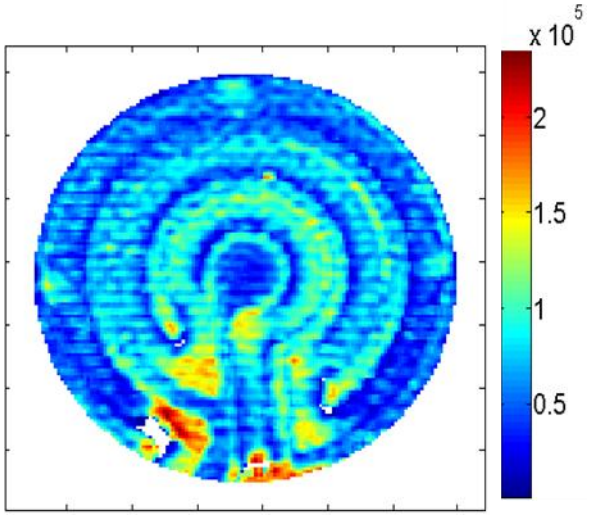

(d)

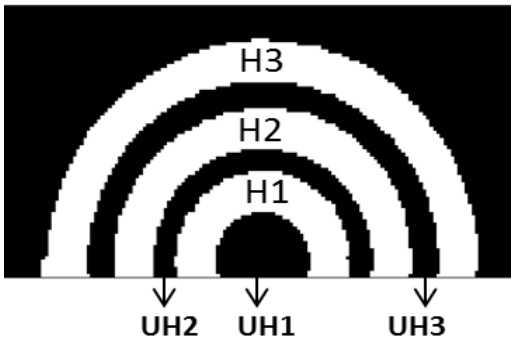

(e)

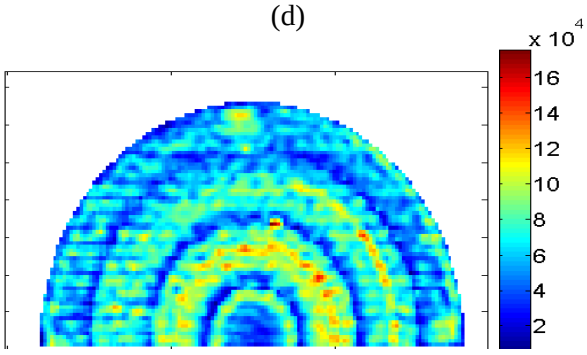

(f)

Figure 5

2.3×10^5 W/m^2	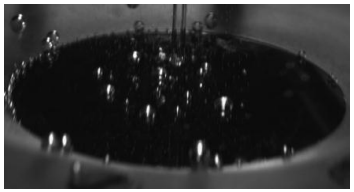 5.1 (a)	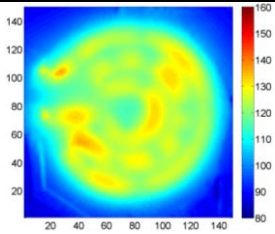 5.1 (b)	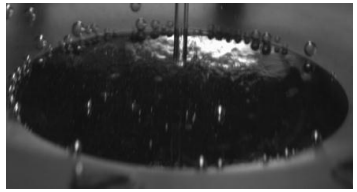 5.1 (e)	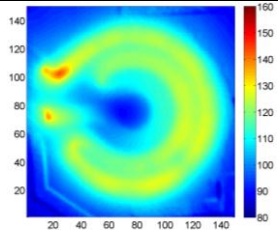 5.1 (f)	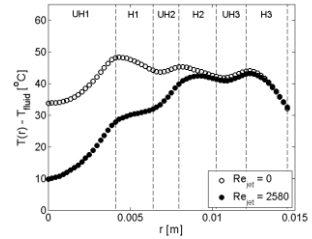 5.1 (i)
	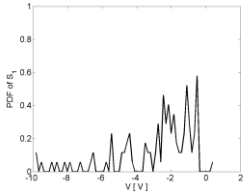 5.1 (c)	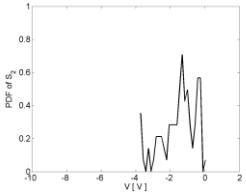 5.1 (d)	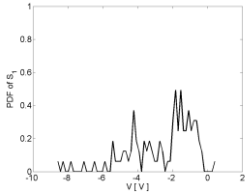 5.1 (g)	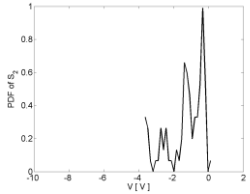 5.1 (h)	
2.9×10^5 W/m^2	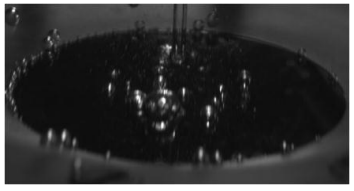 5.2 (a)	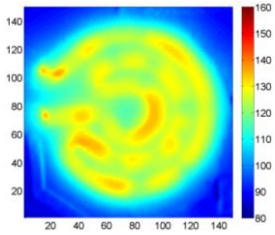 5.2 (b)	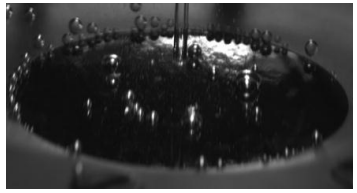 5.2 (e)	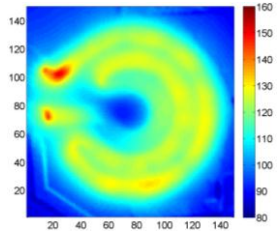 5.2 (f)	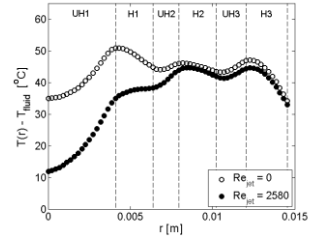 5.2 (i)
6.6×10^5 W/m^2	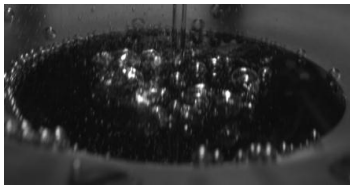 5.3 (a)	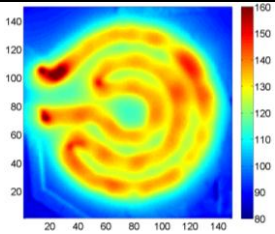 5.3 (b)	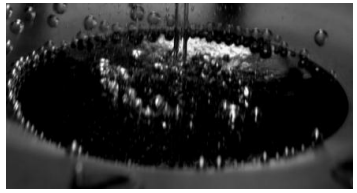 5.3 (e)	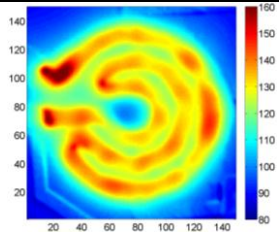 5.3 (f)	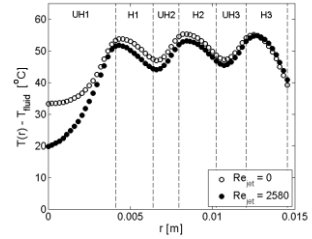 5.3 (i)
	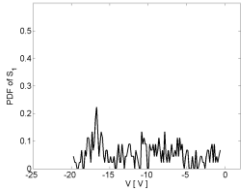 5.3 (c)	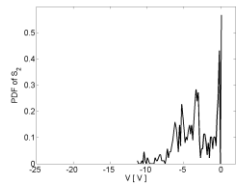 5.3 (d)	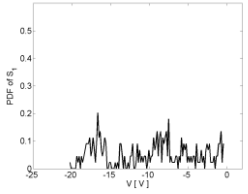 5.3 (g)	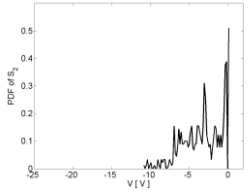 5.3 (h)	

Figure 6

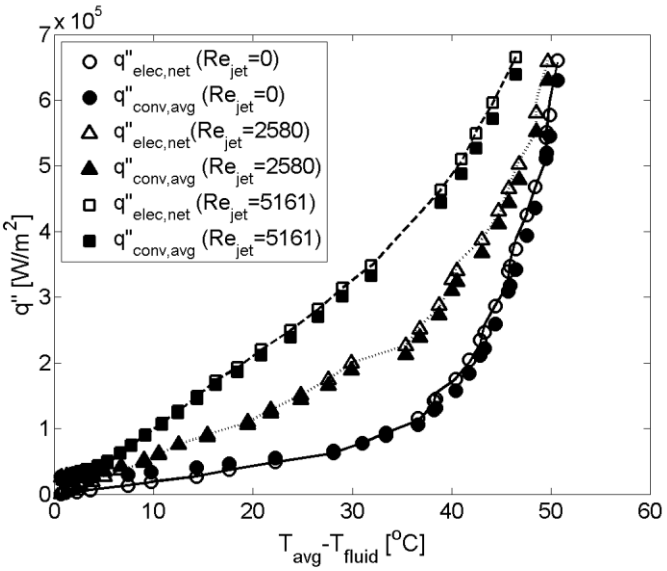
x 10^5
q'' [W/m^2]
T_avg-T_fluid [°C]
q''elec,net (Rejet=0)
q''conv,avg (Rejet=0)
q''elec,net (Rejet=2580)
q''conv,avg (Rejet=2580)
q''elec,net (Rejet=5161)
q''conv,avg (Rejet=5161)

Figure 7

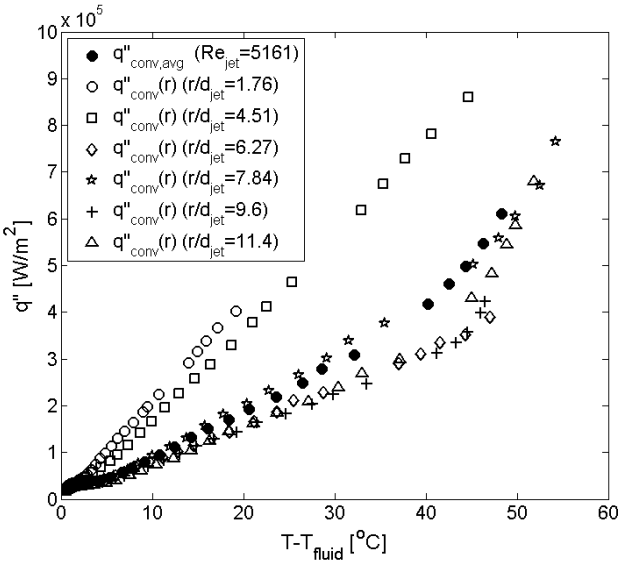
x 10^5
q"conv,avg (Rejet=5161)
q"conv(r) (r/djet=1.76)
q"conv(r) (r/djet=4.51)
q"conv(r) (r/djet=6.27)
q"conv(r) (r/djet=7.84)
q"conv(r) (r/djet=9.6)
q"conv(r) (r/djet=11.4)
q" [W/m2]
T-Tfluid [°C]
0
1
2
3
4
5
6
7
8
9
10
0
10
20
30
40
50
60

Figure 8

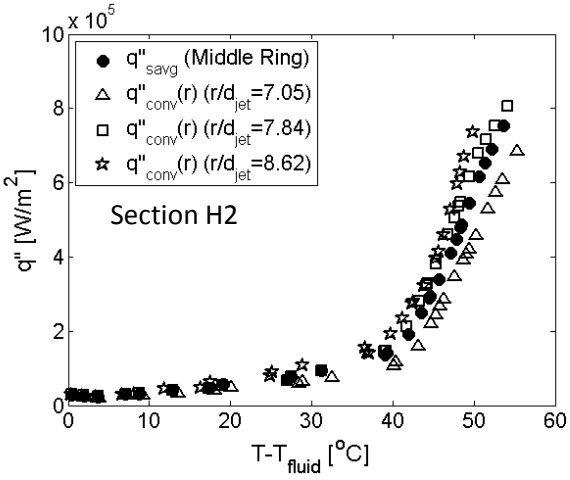

8 (a)

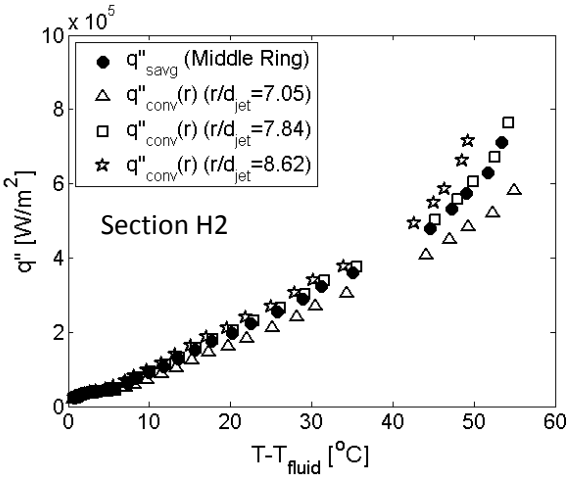

8 (b)

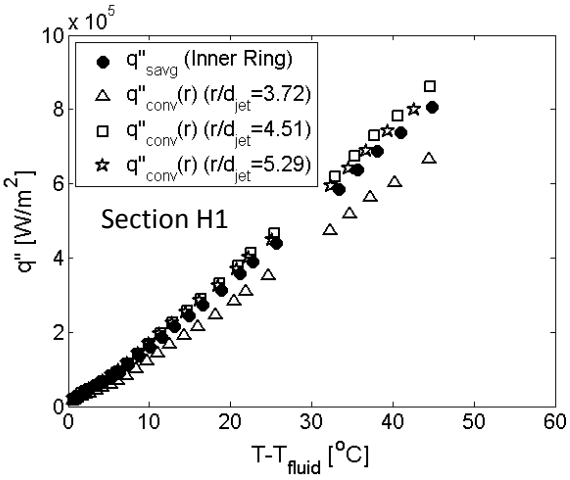

8 (c)

Figure 9

Pool Boiling | **Re_{jet} = 5161**

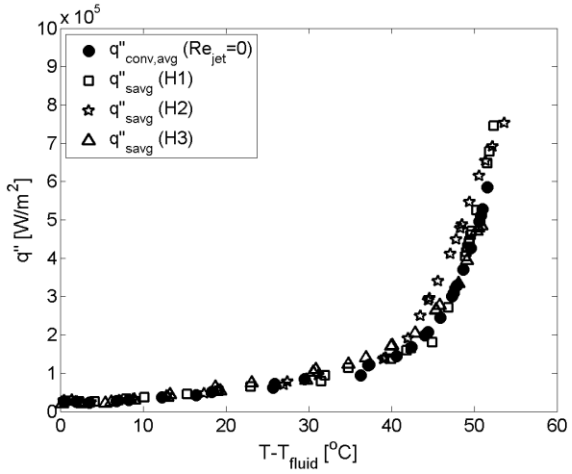

9 (a)

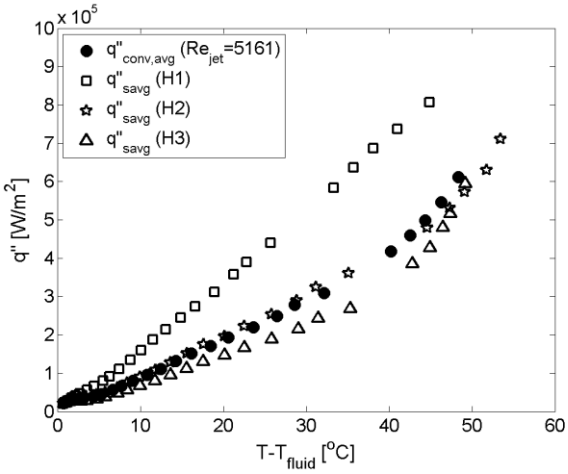

9 (c)

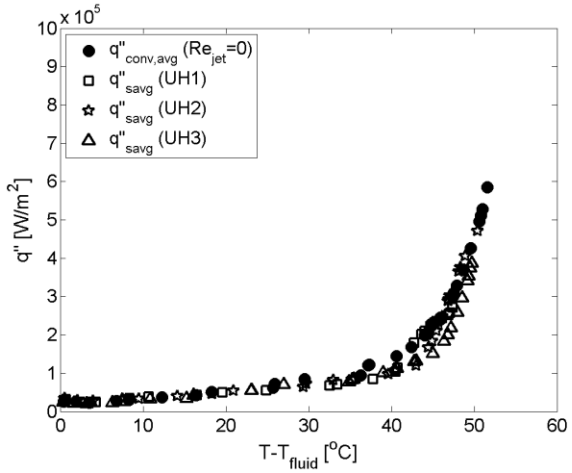

9 (b)

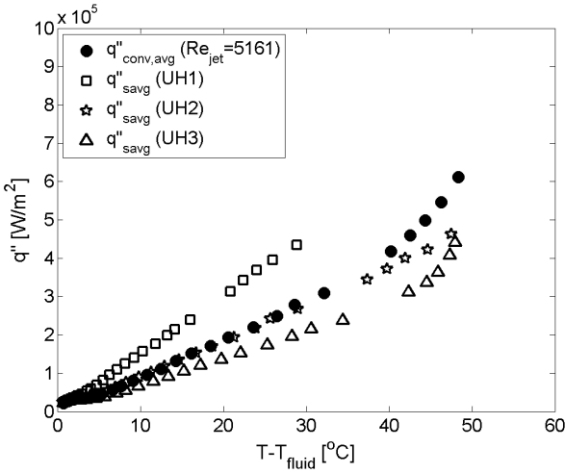

9 (d)

Figure Captions

Fig. 1: Serpentine aluminum heaters and thin-film sensors deposited on the silicon substrate

Fig. 2: Polycarbonate substrate mount

Fig. 3: Test facility schematic

Fig. 4: Steps for IR image reduction shown for an impinging jet non-boiling condition (a) Thermal image filtered using a top-hat filter. Temperature scale in ^{o}C (b) Binary representation of the heater (c) Energy balance on a (pixel) control volume (d) Convective heat flux in W/m^2 (e) symmetric semi-circular region of heater geometry (f) heat flux corresponding to the symmetric semi-circular heat region in W/m^2

Fig. 5: Visualization results and probability distribution functions (PDF) of thin-film sensor for (left) pool boiling (Re_{jet} = 0) and (right) jet impingement boiling (Re_{jet} = 2580), with increasing flux (a) instantaneous high-speed images of boiling activity during pool boiling (b) time averaged filtered temperature maps on the back side of the silicon wafer during pool boiling (c) PDF of S_1 during pool boiling (d) PDF of S_2 during pool boiling (e) instantaneous high-speed images of boiling activity for Re_{jet} = 2580 (f) time averaged filtered temperature maps on the back side of the silicon wafer for Re_{jet} = 2580 (g) PDF of S_1 for Re_{jet} = 2580 (h) PDF of S_2 for Re_{jet} = 2580 (i) Comparison of radial temperature difference profiles for pool boiling and Re_{jet} = 2580

Fig. 6: Comparison of the net input electrical heat flux with area-averaged heat flux values plotted as function of area-averaged temperature difference

Fig. 7: Local versus area-averaged boiling curves for Re_{jet} = 5161

Fig. 8: Local versus sectionally-averaged boiling curves for (a) pool boiling - heated section H2 (b) Re_{jet} = 5161- heated section H2 (c) Re_{jet} = 5161- heated section H1

Fig. 9: Sectionally-averaged boiling curves for pool boiling (left) and Re_{jet} = 5161 (right) plotted for heated sections (H1, H2 and H3) on the heater rings (top row) and unheated section (UH1, UH2, and UH3) off the heater rings (bottom row)